OVMS-plus at the LBT. Disturbance compensation simplified.

Michael Böhm[a,b], Jörg-Uwe Pott[b], Jose Borelli[b], Phil Hinz[c], Denis Defrère[c,e], Elwood Downey[c], John Hill[d], Kellee Summers[d], Al Conrad[d], Martin Kürster[b], Tom Herbst[b], Oliver Sawodny[a]

[a]ISYS, University of Stuttgart, Pfaffenwaldring 9, 70569 Stuttgart, Germany
[b]Max-Planck-Institute for Astronomy, Königstuhl 17, 69117 Heidelberg, Germany
[c]Steward Observatory, University of Arizona, 933 N. Cherry Ave, Tucson, AZ 85721, USA
[d]LBTO, 933 N. Cherry Ave, Tucson, AZ 85721, USA
[e]STAR Research Unit, Université de Liège, Allée du Six Août, 4000 Liège, Belgium

ABSTRACT

In this paper we will briefly revisit the optical vibration measurement system (OVMS) at the Large Binocular Telescope (LBT) and how these values are used for disturbance compensation and particularly for the LBT Interferometer (LBTI) and the LBT Interferometric Camera for Near-Infrared and Visible Adaptive Interferometry for Astronomy (LINC-NIRVANA). We present the now centralized software architecture, called OVMS$^+$, on which our approach is based and illustrate several challenges faced during the implementation phase. Finally, we will present measurement results from LBTI proving the effectiveness of the approach and the ability to compensate for a large fraction of the telescope induced vibrations.

Keywords: Large Binocular Telescope, Accelerometer, Estimation, Delay, Control, Feedforward Control, Vibration, LBTI, LINC-NIRVANA

1. INTRODUCTION

Large ground-based telescopes have undergone tremendous growth in size in the past decades. Today, the largest single monolithic mirrors for telescopes have diameters of approximately 8 m, which constitutes a technical limit. Thus, some past and most future telescope projects going beyond the 8 m-class rather utilize an array of single mirrors to increase the effective resolution. One of these is the Large Binocular Telescope (LBT) located near Tucson, Arizona (USA), which is equipped with two large 8.4 m primary mirrors. It is shown in Fig. 1. The light

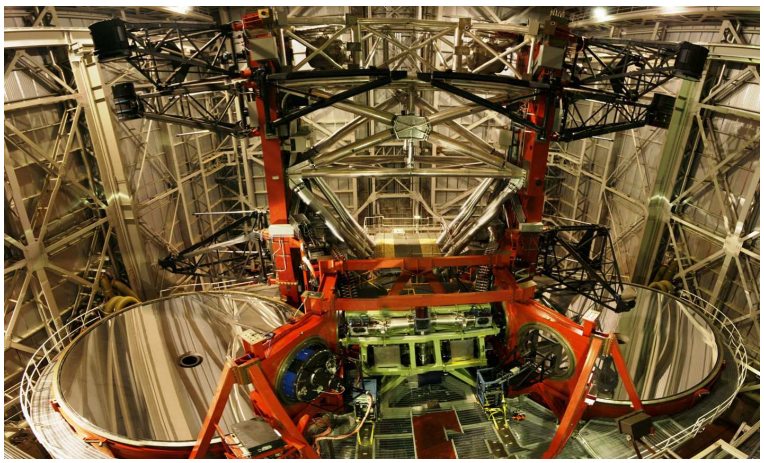

Figure 1: Inner part of the LBT with its symmetrical layout.

Send correspondece to Michael Böhm (boehm@isys.uni-stuttgart.de)

Ground-based and Airborne Telescopes VI, edited by Helen J. Hall, Roberto Gilmozzi, Heather K. Marshall,
Proc. of SPIE Vol. 9906, 99062R · © 2016 SPIE · CCC code: 0277-786X/16/$18 · doi: 10.1117/12.2231268

collected by both primary mirrors is reflected via the adaptive secondary mirrors and tertiary mirrors into one of the center positioned instruments. There will be two interferometers installed at the LBT eventually, where one is the **N**ear-**I**nfra**R**ed/**V**isible **A**daptive Camera and I**N**terferometer for **A**stronomy (LINC-NIRVANA), which is currently being installed and is described in Herbst et. al.,[1] while the other is the **L**arge **B**inocular **T**elescope **I**nterferometer (LBTI), which is described in more detail for example in Hinz et. al.[2] and is in operation at the LBT since 2010. Due to wind excitation at the telescope, the optically identical sides of the telescope move in a slightly different, somewhat randomly disturbed way. These mechanical disturbance due to vibration mainly lead to low order aberrations of piston, tip, and tilt for the single telescope mirrors. While tip and tilt can in theory be corrected by a fast adaptive optics (AO) control loop, the AO is not sensible to piston. However, the difference in piston between the telescope sides, the **o**ptical **p**athway **d**ifference (OPD), needs to remain at a very small level at beam combination in order to enable fringe tracking for the respective interferometer. Thus, need arises for an opto-mechanical device to correct this OPD difference to keep both light paths co-phased. For LINC-NIRVANA, this device is a position-controlled piezo motor with a travel range of 75 µm, while LBTI has chosen a tweeter-woofer setup, with one corrector for slow, but large differences and one corrector for fast but small differences. The latter will be used to correct mechanical vibrations, which are typically in the order of several µm and above 10 Hz.[3]

In order to measure the disturbances, the LBT main mirrors are equipped with 5 accelerometers each, which are of piezo-type and supplied by PCB electronics. The analog accelerometer values are converted to digital values in a PowerPC, called PowerDNR RackTangle, which is equipped with 12 DNR-AI-211 cards, all supplied by UEI. This device can digitize 48 analog channels and send the values via GBit-ethernet. At the LBT, the 48 values and a time stamp are send out using UDP-Multicast. Each client in the network can possibly subscribe to the multicast feed. The system is completed by a GUI, which is basically a plotting tool to visualize the current measurements and a telemetry client taking care of archiving the data in the standard HDF5 file format. All of this is referred to as the **o**ptical **v**ibration **m**easurement **s**ystem (OVMS), which is described in Kürster et. al.[4]

This system has been in operation since 2009 and delivers stable and reliable data since its commissioning in March 2013. However, its use was mainly limited to engineers in the search for vibrations sources at the LBT, and possible options for their mitigation and telescope enhancements. For instrument scientists and their specific need of a flexible, fast and easy to use system, a solution was yet to be found. On top of this, the calculation of the actual mirror motion from the accelerometer values was left to every instrument's control loop. In hindsight, this does not seem reasonable. To increase synergy between using and testing OVMS with different instruments, we now implemented a centralized calculation of OPD, tip and tilt, as these calculations do not rely on instrument specific parameters. We present now in this paper a solution which not only estimates the differential OPD (and also tip and tilt values) from the accelerometer readings, but also offers a simple and flexible use to the instrument scientists, for which it is eventually intended. Additionally, this system can be used for feedforward correction of mechanically originated tip and tilt disturbances to the adaptive secondaries and thus also offers a benefit not only to the interferometers at the LBT, but to all instruments that make use of LBTs adaptive optics capabilities. Because our solution is based on the OVMS, but greatly enhances its capabilities, it has been called $OVMS^{+}$.

The paper will focus on the basics of the implemented algorithm in section 2. This is followed by a description of changes and additions that we have made to the OVMS software in section 3. At the end, we present and discuss on sky measurements illustrating the performance of the new disturbance estimation and compensation.

2. ALGORITHM

In order to make use of the disturbance compensation, the actual OPD has to be calculated from the accelerometer measurements. For this, we have a dynamic system, called *estimator*, which is essentially a linear filter. The estimator is designed to match the double integration very well for a specific frequency range of 8 Hz to 60 Hz, in which most of the relevant mechanical vibrations at the LBT occur. Small frequencies representing offsets and drifts have to be attenuated by this filter. The filter is designed for optimal performance at a sampling rate of 1 ms. The presented algorithm is based on recently published results.[5,6]

As illustrated by Figure 2, the estimation algorithm can be divided into two steps. First, the measurements are integrated by the dynamic estimator to find the position values of the mirrors at the accelerometer locations. These values can then be used to find the actual piston, tip, and tilt values of the respective mirror.

Figure 2: The estimation algorithm can be devided into two steps: integration of the measurements and geometric transformation of the positions to derive the low order aberrations.

2.1 Integration

The broadband filtering aims at approximating the double integrating behaviour for a specific frequency range. The estimation filter is based on two lowpass filters $G_L(s)$ and three highpass filters $G_H(s)$. It is supplemented with two lead lag elements $G_{\mathrm{ll},1}$ and $G_{\mathrm{ll},2}$, which are introduced to reduce the phase error in the low frequency regime around 8 Hz and bring it closer to the ideal $-180°$, and to compensate the phase drop for higher frequencies due to discretization, respectively. The effect of $G_{\mathrm{ll}2}$ on the overall transfer function degrades at higher sample rates, and it can be omitted for sample rates of 2 kHz or more. Details on these individual filters can be found in Böhm et. al.[5] The overall filter transfer function G_{F} is then given by:

$$\begin{aligned} G_{\mathrm{F}}(s) &= G_{\mathrm{H}}(s)\, G_{\mathrm{L}}(s)\, G_{\mathrm{H}}(s)\, G_{\mathrm{L}}(s)\, G_{\mathrm{H}}(s)\, G_{\mathrm{ll},1}(s)\, G_{\mathrm{ll},2}(s) \\ &= G_{\mathrm{H}}^3(s)\, G_{\mathrm{L}}^2(s)\, G_{\mathrm{ll},1}(s)\, G_{\mathrm{ll},2}(s). \\ &= \left(\frac{s}{s+\pi}\right)^3 \left(\frac{1}{s+3\pi}\right)^2 \frac{s+10\pi}{s+0.6\pi}\,\frac{s+98\pi}{s+103\pi} \end{aligned} \tag{1}$$

Thus, with the estimated position $z(t)$ and the measured acceleration $y_{\mathrm{acc}}(t)$, it holds:

$$Z(s) = G_{\mathrm{F}}(s) Y_{\mathrm{acc}}(s). \tag{2}$$

The bode diagram for $G_{\mathrm{F}}(s)$ is shown in Fig. 3. The estimation filter from equation (1) can be rewritten in state

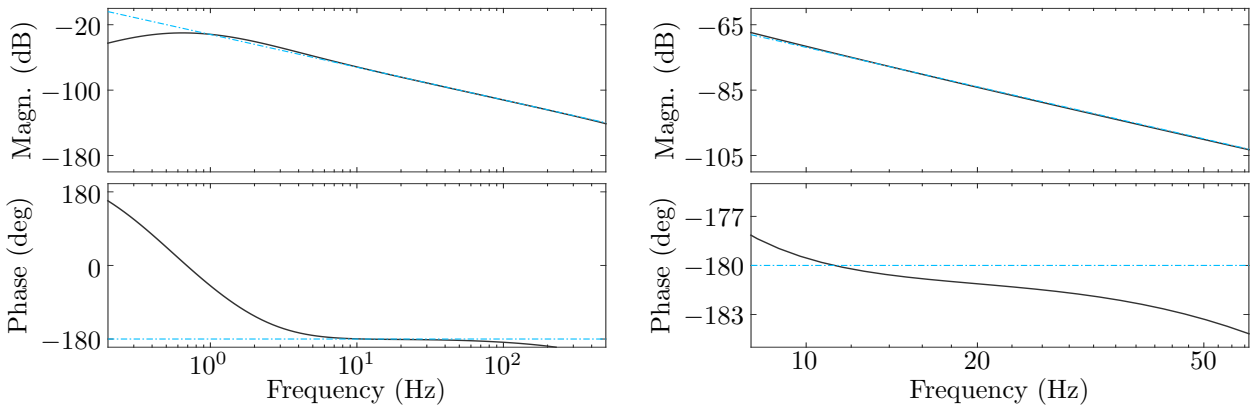

Figure 3: Bode Diagramm for the broadband filter $G_F(s)$, comparing the ideal double integrator (dash-dotted blue) with the designed filter used for position estimation (solid dark) in the complete frequency range (left) and for the desired frequency range of 8 Hz to 60 Hz (right).

space notation:

$$\begin{aligned} \dot{\hat{\boldsymbol{\xi}}}(t) &= \boldsymbol{A}\hat{\boldsymbol{\xi}}(t) + \boldsymbol{B} y_{\mathrm{acc}}(t) \\ z(t) &= \boldsymbol{C}\hat{\boldsymbol{\xi}}(t). \end{aligned} \tag{3}$$

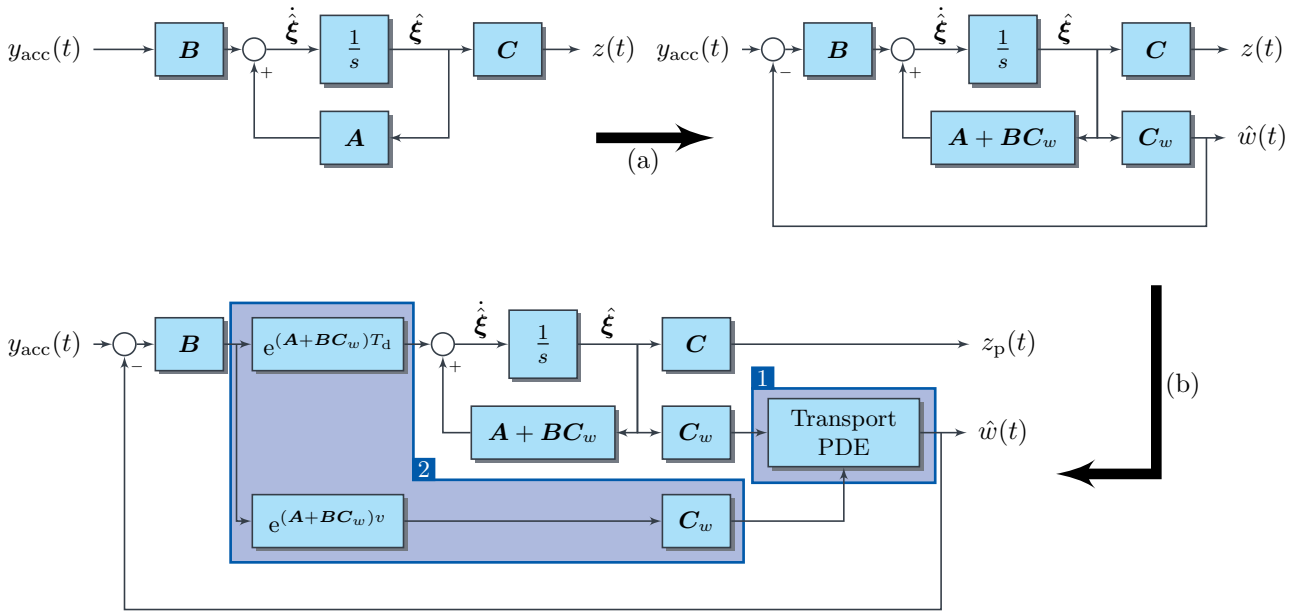

Figure 4: (a) Transformation of the observer scheme (3) into (4) and (b) extension to the full delay compensating observer scheme (7) featuring additional measurement delay (blue box 1) and the delay compensating extensions to the original observer feedback (blue box 2).

This filter is now extended by a delay compensation, which is described in a publication currently under review.[6] This is necessary, because due to the distribution using the UDP-Multicast protocol, the estimated values are subject to a delay of approximately $T_\mathrm{d} = 3\,\mathrm{ms}$. Without compensation, for a 24 Hz sine disturbance, the *best case* residual error will remain at about 40 % of the original value, which illustrates the importance of a delay compensation algorithm. In the following, we will sketch the main idea for the derivation.

To compensate the delay, the estimator from equation (3) has to be extended in order to increase the phase in the desired frequency regime. The method we choose to derive such an extended estimator is backstepping applied to a transport PDE representing the measurement delay and cascaded with a virtual system, which is extracted from the original disturbance estimator (3). This method has been published,[7] but instead of an actual plant model, we extract a virtual model from our estimator. For this, let us rewrite the estimator given in (3) in a Luenberger observer scheme:[8]

$$\begin{aligned}\dot{\hat{\boldsymbol{\xi}}}(t) &= (\boldsymbol{A}+\boldsymbol{B}\boldsymbol{C}_w)\,\hat{\boldsymbol{\xi}}(t) + \boldsymbol{B}\left(y_\mathrm{acc}(t) - \boldsymbol{C}_w\hat{\boldsymbol{\xi}}(t)\right),\\ \hat{w}(t) &= \boldsymbol{C}_w\hat{\boldsymbol{\xi}}(t),\\ z(t) &= \boldsymbol{C}\hat{\boldsymbol{\xi}}(t),\end{aligned} \tag{4}$$

with $\boldsymbol{C}_z = [-1,0,0,0,0,0,0]$. This choice of $\boldsymbol{C}_z$ guarantees the stability of the observed autonomous system

$$\begin{aligned}\dot{\boldsymbol{\xi}}(t) &= (\boldsymbol{A}+\boldsymbol{B}\boldsymbol{C}_w)\,\boldsymbol{\xi}(t)\\ w(t) &= \boldsymbol{C}_w\boldsymbol{\xi}(t).\end{aligned} \tag{5}$$

due to the structure of $\boldsymbol{A}$ (lower triangular).[6] The transformation from (3) to (4) is illustrated in Figure 4(a).

The measurement delay T_d described by a transport PDE is now appended to the output of the autonomous

system (5):

$$\begin{aligned}\dot{\boldsymbol{\xi}}(t) &= (\boldsymbol{A} + \boldsymbol{B}\boldsymbol{C}_w)\,\boldsymbol{\xi}(t)\\ u(T_\mathrm{d}, t) &= \boldsymbol{C}_w\boldsymbol{\xi}(t),\\ \partial_t u(v,t) &= \partial_v u(v,t),\\ w(t) &= u(0,t).\end{aligned} \tag{6}$$

with $u(v,t) \in [0, T_\mathrm{d}] \times [0,\infty)$ being a distributed state to model the infinite dimensional delay T_d. The partial derivatives with respect to t and v are denoted by ∂_t and ∂_v, respectively. The following observer then guarantees asymptotically stable observer error dynamics:[7]

$$\begin{aligned}\dot{\hat{\boldsymbol{\xi}}}(t) &= (\boldsymbol{A} + \boldsymbol{B}\boldsymbol{C}_w)\,\hat{\boldsymbol{\xi}}(t) + \mathrm{e}^{(\boldsymbol{A}+\boldsymbol{B}\boldsymbol{C}_w)T_\mathrm{d}}\,\boldsymbol{B}\left(y_\mathrm{acc}(t) - \hat{w}(t)\right),\\ \partial_t\hat{u}(v,t) &= \partial_v\hat{u}(v,t) + \boldsymbol{C}_w\,\mathrm{e}^{(\boldsymbol{A}+\boldsymbol{B}\boldsymbol{C}_w)v}\,\boldsymbol{B}\left(y_\mathrm{acc}(t) - \hat{w}(t)\right),\\ \hat{u}(T_\mathrm{d}, t) &= \boldsymbol{C}_w\hat{\boldsymbol{\xi}}(t),\\ \hat{w}(t) &= \hat{u}(0,t).\end{aligned} \tag{7}$$

In order to get a predicted estimate of $z(t)$, called $z_\mathrm{p}(t)$, the estimated state $\hat{\boldsymbol{\xi}}(t)$ can be used with:

$$z_\mathrm{p}(t) = \boldsymbol{C}\hat{\boldsymbol{\xi}}(t). \tag{8}$$

A comparison of the delay compensating and the original observer is shown in Figure 4(b). The additional Transport PDE can be seen on the right modeling the measurement delay. Because the PDE state has to be estimated as well, the extension is shown in the second box with the prediction $\mathrm{e}^{(\boldsymbol{A}+\boldsymbol{B}\boldsymbol{C}_w)T_\mathrm{d}}$ for the ODE observer, and the distributed prediction $\mathrm{e}^{(\boldsymbol{A}+\boldsymbol{B}\boldsymbol{C}_w)v}$ for the PDE part of the observer. For implementation, the observer scheme from equation (7) is discretized in space and used in its time discrete state space representation.

2.2 Transformation

First, the values acquired in the integration step have to be transformed into tip, tilt and piston values for the individual mirrors. For this, we look first at the inverse problem: the calculation of the sensor displacement from known mirror translation (d - OPD), rotation around the x-axis (φ_x - tip), and rotation around the y-axis (φ_y - tilt). For mirror k, the displacement of sensor i can be calculated using the sensor coordinates (x_i, y_i) along with the geometric constraints, which yields:

$$z_{i,k} = d_k + y_{i,k}\varphi_{x,k} - x_{i,k}\varphi_{y,k} \tag{9}$$

Since tip and tilt angles at the LBT are small, this linear relationship can be used. For a number of n_k sensors measuring along the z-axis (i. e. perpendicular to the optical surface), this can be summarized as follows:

$$\begin{pmatrix} z_{1,k}\\ z_{2,k}\\ \vdots\\ z_{n_k,k}\end{pmatrix} = \underbrace{\begin{pmatrix} y_{1,k} & -x_{1,k} & 1\\ y_{2,k} & -x_{2,k} & 1\\ & \vdots & \\ y_{n_k,k} & -x_{n_k,k} & 1\end{pmatrix}}_{=\boldsymbol{T}_k} \begin{pmatrix}\varphi_{x,k}\\ \varphi_{y,k}\\ d_k\end{pmatrix} \tag{10}$$

As can be seen, the matrix $\boldsymbol{T}_k$ contains the sensor positions of the n_k sensors of the k-th mirror. This set of algebraic equations can be solved using the (pseudo-)inverse of the matrix $\boldsymbol{T}_k$ in the case of $n_k \geq 3$:

$$\begin{pmatrix}\varphi_{x,k}\\ \varphi_{y,k}\\ d_k\end{pmatrix} = \boldsymbol{T}_k^{+} \begin{pmatrix} z_{1,k}\\ z_{2,k}\\ \vdots\\ z_{n_k,k}\end{pmatrix}. \tag{11}$$

For less than 3 sensors, the set of equations is undertermined and cannot be solved.

Additionally, these values have to be converted into a common reference frame for which the respective sensitivities have to be known. This is necessary especially for tip and tilt angles, because e. g. a 1 mas tilt angle of M1 has to be corrected by a different tilt angle at M2. A very suited common reference frame is the instrument focal plane, because it also considers the respective rotation of M3, which is specific to the instrument.

3. SOFTWARE ARCHITECTURE

Before OVMS$^+$, the OVMS software at the LBT had 3 basic parts. The software on the UEI RackTangle is used to read the AD-Conversion cards and distribute the values along with a correspnding time stamp via UDP-Multicast. The GUI runs on a seperate linux computer in the operator control room of the LBT and visualizes the measurements on large screens. Last, the telemetry is used to read the UDP stream and write the values to an archive in HDF5 file format. This is visualized in Figure 5. Because the new estimation software runs on

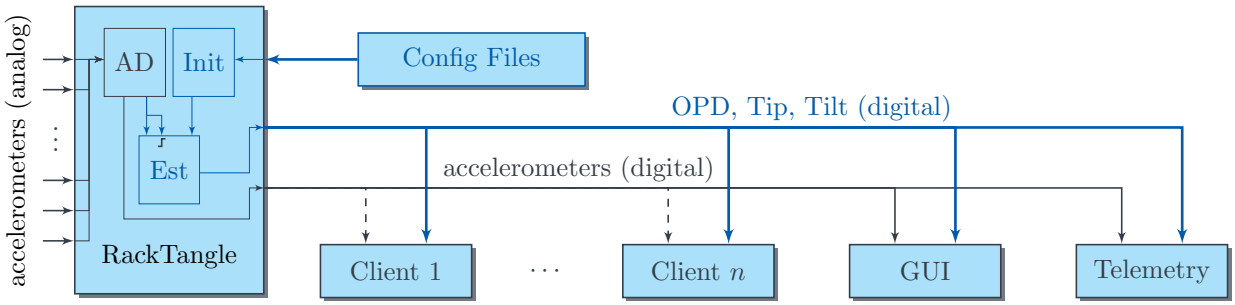

Figure 5: Overview of the software architecture of OVMS (black) and OVMS$^+$ (blue extension). While the software's AD module is not changed, two new modules have been added. The initialization parses the config-files to calculate the estimator structure, which is then used in the estimation module. The estimation is triggered by the AD module, whereas the initialization is called only once at startup.

the PowerPC UEI RACKtangle, the architecture of OVMS$^+$ and the original architecture are very similar. The multicast buffer, which is sent at a constant sample rate, has now been appended with the estimated values.

One of the challenges during implementation was to supply a software, from which both the engineers, and the instrument scientists and astronomers could benefit. Thus, there are basically two important modes in which the software can be run. In the *instrument mode*, the software calculates 5 values: the differential piston (= OPD) and the equivalent focal plane motion resulting from the tip and tilt angles of the three main mirrors for each side of the telescope. In the *engineering mode*, the software calculates 18 values: the piston, tip and tilt motion for all six main mirrors. This mode needs more ressources on the PowerPC and thus runs at a maximum sample speed of 1300 Hz when used with the delay compensation. For science use, the better accuracy of higher sampling rates might be needed, while the LBTO engineers are very much interested in the more on information of this mode. Additionally, there is a *compatibility mode*, where the software behaves as the original OVMS software and no additional values are sent. The mode can be chosen upon startup of the service by the user. The prediction time as a parameter to the delay compensation can also be set by the user upon startup.

When the service starts, the estimator is initialized and then used in the actual estimation function, which is triggered by the A/D-conversion of the sensor signals and therefore runs at the specified sample rate. Usually, the sample rate is $T_{\text{sample}} = 1\,\text{ms}$, however, lower or higher values can be set if desired. For the initialization of the estimation, two configuration files are needed. One specifies the location, calibration data and channel number for each accelerometer for each of the six mirrors. These values presumably do not change very often and will be mainly maintained by LBTO personnel, e. g. after the replacement of a broken sensor or after mounting additional sensors. The second config file contains several instrument specific parameters, i. e. the focal plane sensitivities of the main mirrors, which depend on the optics and the initial focal ratio of the secondary. Also, the angle of M3 is different for different instruments, which can be set in this file.

4. RESULTS

Measurements taken with LBTI on March 5, 08:01 - 08:22 UTC, illustrate the performance of the presented algorithm. Three typical sequences of 3 s are compared in Figure 6. Note that the OVMS$^+$-software was

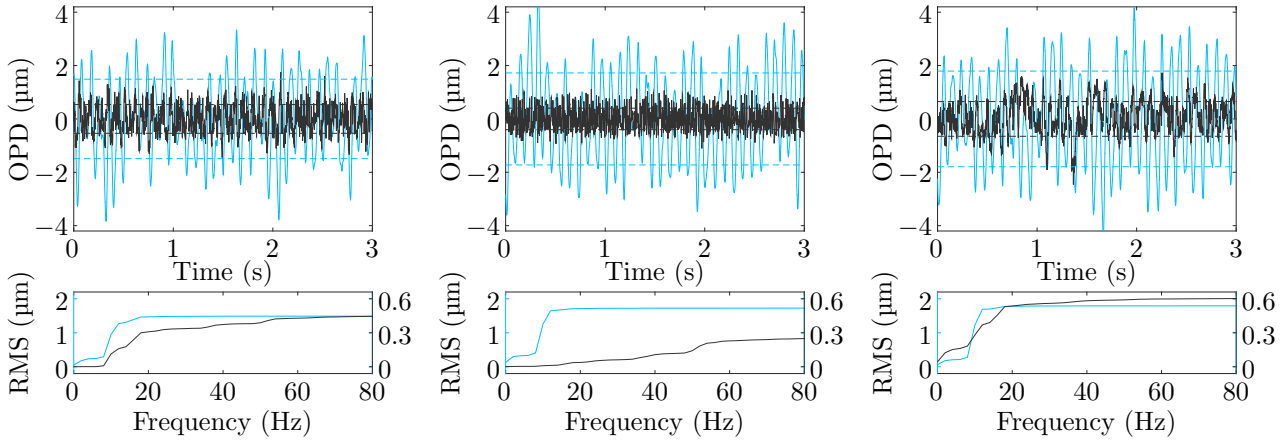

(a) OVMS$^+$ OFF, $K_i = 300$ (b) OVMS$^+$ ON, $K_i = 300$ (c) OVMS$^+$ ON, $K_i = 30$

Figure 6: Time series and cumulated power spectrum of the estimated OPD (blue) and the closed loop residual error (black). Note the two different scales in the spectrum plots for better comparison, with the left axis showing the spectrum of the estimated OPD, and the right axis that of the residual OPD. On the left, there is pure feedback action, in the middle a combination of feedback and disturbance feedforward is used. On the right, the feedback integral gain is reduced by a factor of 10. Without OVMS$^+$ feedforward, the RMS (shown as dashed lines) is reduced from 1489 nm to 539 nm (-64 %), while with OVMS$^+$ feedforward the OPD residual is reduced from 1724 nm down to 403 nm (-77 %). Thus, the combination of both reduces the input disturbance RMS by about a factor of 4.5. Using OVMS$^+$ feedforward, but a much smaller feedback gain restores the performance of the original pure feedback system with a reduction from 1793 nm to 651 nm (-64 %).

operating without the delay compensation, although this feature is ready to use. However, since it is less critical for LBTI, most tests have been carried out without this option. However, as can be seen in Figure 6c, when using OVMS$^+$ with a small gain in the feedback loop, there are significant residuals between 8 Hz and 60 Hz, especially around 12 Hz and 18 Hz, which are at $\approx$ 30 % of the estimated OPD. Since these are modes of M2 and M3, there is some potential to further decrease this using the prediction mode to compensate for the measurement delay of about 3 ms.

Also, the LBTI feedback loop was not fully optimized for this demonstration, so the feedback performance shown here does not represent LBTI's best PHASECam control loop performance. Nevertheless, the performance gained by using OVMS$^+$ could be demonstrated. Later tests suggested about 15 % lower closed loop residual with an optimized LBTI feedback loop.

As can be seen in Figure 6a, the pure integral feedback of the LBTI PHASECam[9] reduces the residual to 36 % of the estimated OPD. However, there are still significant low frequency components around 10 Hz - 20 Hz in the residual OPD. These components can be further reduced to a residual OPD of 23 % of the estimated OPD by using the estimation provided by OVMS$^+$ as feedforward input to the fast pathlength corrector of LBTI, ref. Figure 6b. As illustrated, only high frequency components above 40 Hz remain. There is a very strong disturbance frequency around 50 Hz, which is visible in the PHASECam data, but not in the OVMS data. Thus, its source must be located within the LBTI instrument, which renders corrected by OVMS$^+$ feedforward impossible, unless the responsible part is identified and equipped with additional accelerometers. Preliminary tests suggest that it is related to some resonance of the correction device, which seems to be excited more with larger feedback gains. This theory is also supported by the comparison of Figure 6a and 6b with Figure 6c. The extended spectrum of the residual error suggests additional internal resonances at 90 Hz, 115 Hz, and just below 170 Hz.

Using OVMS$^+$ feedforward, it is also possible to reduce the feedback integral gain without increasing the residual error. As can be seen in Figure 6c, despite a reduction of the feedback integral gain from $K_i = 300$ to $K_i = 30$, the residual OPD remains at 36 % of the estimated OPD when using the OVMS$^+$ feedforward. This is very important, as a smaller gain increases the robustness of the feedback loop, which is crucial for longtime stability during observations. When using OVMS$^+$ with a reduced feedback gain, a major part of the residual error is due to very low frequency drifts below 8 Hz, which are not estimated by the OVMS$^+$ algorithm.

In general, when using OVMS$^+$ with LBTI, most of the remaining residual OPD is due to unregarded corrector dynamics and unmeasured vibration of the instrument optics. The estimation error of OVMS$^+$ should remain below 8 %,[5] and the error due to intrinsic sensor noise is negligible.

5. CONCLUSION

With OVMS$^+$, the LBT is now equipped with a system to calculate piston, tip, and tilt values for all its main mirrors in real time, aggregate these and deliver differential piston, as well as focal plane motion due to tip and tilt angles. These values are sent via UPD multicast over ethernet and thus are easily accessible for any of the instruments or the observatory engineers. Additionally, the software supports a prediction mode to compensate for small delays up to 10 ms.

The calculated differential piston has been used by LBTI and the effectiveness of OVMS$^+$ has been demonstrated. With pure feedback, the OPD residual RMS was at 36 % of the estimated OPD RMS. This could be reduced using OVMS$^+$ without any other changes to 23 %. Also, the performance could be preserved at a 36 % residual RMS by use of OVMS$^+$ with a much smaller (factor of 10) feedback gain, which significantly improves loop stability, robustness and thus integration time. Overall, with the experience of a handfull of LBTI runs this year using and testing the OVMS$^+$ system, it can be concluded that OVMS$^+$ is very beneficial to the LBTI team and will also be beneficial to LINC-NIRVANA, which is currently being installed at the LBT.

REFERENCES

[1] T. M. Herbst, R. Ragazzoni, A. Eckart, and G. Weigelt, "LINC-NIRVANA: achieving 10 mas imagery on the Large Binocular Telescope," in *Society of Photo-Optical Instrumentation Engineers (SPIE) Conference Series*, *Society of Photo-Optical Instrumentation Engineers (SPIE) Conference Series* **7014**, Aug. 2008.

[2] P. M. Hinz, T. Connors, T. McMahon, A. Cheng, C. Y. Peng, W. Hoffmann, D. McCarthy, Jr., and R. Angel, "Large binocular telescope interferometer: the universal beam combiner," in *Proc. SPIE*, **5491**, pp. 787–797, 2004.

[3] M. Böhm, J.-U. Pott, M. Kürster, and O. Sawodny, "Modeling and Identification of the Optical Path at ELTs - a Case Study at the LBT," in *Proc. of the 6th IFAC Symposium on Mechatronic Systems*, *Proc. of the 6th IFAC Symposium on Mechatronic Systems* **6**, pp. 249–255, April 2013.

[4] M. Kürster, T. Bertram, J. L. Borelli, M. Brix, W. Gässler, T. M. Herbst, V. Naranjo, J.-U. Pott, and J. Trowitzsch, "OVMS: the optical path difference and vibration monitoring system for the LBT and its interferometers," in *Proc. of SPIE*, **7734**, July 2010.

[5] M. Böhm, J.-U. Pott, O. Sawodny, T. Herbst, and M. Kürster, "Real-Time Vibration Compensation for Large Telescopes," *Monthly Notices of the Royal Astronomical Society* **442**(3), pp. 2446–2455, 2014.

[6] M. Böhm, J.-U. Pott, M. Kürster, O. Sawodny, D. Defrére, and P. Hinz, "Delay Compensation for Real Time Disturbance Estimation at Extremely Large Telescopes," *IEEE Transactions on Control Systems Technology* **xx**(x), pp. xxx–xxx, 2016. (under review).

[7] M. Krstic, *Delay Compensation for Nonlinear, Adaptive, and PDE Systems*, Birkhäuser, 2009.

[8] D. Luenberger, "Observing the State of a Linear System," *Military Electronics, IEEE Transactions on* **8**, pp. 74–80, April 1964.

[9] D. Defrére, P. Hinz, E. Downey, D. Ashby, V. Bailey, G. Brusa, J. Christou, W. C. Danchi, P. Grenz, J. M. Hill, W. F. Hoffmann, J. Leisenring, J. Lozi, T. McMahon, B. Mennesson, R. Millan-Gabet, M. Montoya, K. Powell, A. Skemer, V. Vaitheeswaran, A. Vaz, and C. Veillet, "Co-phasing the Large Binocular Telescope: status and performance of LBTI/PHASECam," in *Proc. SPIE*, *Proc. SPIE* **9146**, pp. 914609–914609–8, 2014.